SBA-15-Supported Mixed-Metal Oxides: Partial Hydrolytic Sol−Gel Synthesis, Adsorption, and Structural Properties

Pasquale F. Fulvio,[†] Stanisław Pikus,[‡] and Mietek Jaroniec*,[†]

Department of Chemistry, Kent State University, Kent, Ohio 44242, and Department of Crystallography, M. Curie-Skodowska University, 20-031 Lublin, Poland

ABSTRACT Several bimetallic mixed oxides−silica nanocomposites were prepared using SBA-15 as a support and suitable metal-containing reagents. The oxide precursors were obtained by reacting two metal alkoxides, namely, titanium(IV) isopropoxide [Ti(O^{i}Pr)$_4$], zirconium propoxide [Zr(OPr)$_4$], and aluminum isopropoxide [Al(O^{i}Pr)$_3$], or one of these alkoxides with a solution of nickel nitrate hexahydrate [Ni(NO$_3$)$_2$ · 6H$_2$O] in isopropyl alcohol (^{i}PrOH). The final condensation of the bimetallic species was achieved by a partial hydrolytic sol−gel route in the pores of SBA-15 silica using small amounts of HCl with concomitant slow evaporation of the solvent. High loadings of these oxides were deposited after several deposition cycles. The as-prepared nanocomposites were characterized by thermogravimetric analysis, whereas nitrogen adsorption at −196 °C was measured for the materials calcined at 300 and 600 °C. Nitrogen adsorption isotherms and the calculated pore-size distributions showed that the deposition of large amounts of the aforementioned oxides in SBA-15 occurred according to an "island-type" mechanism, resulting in the formation of pore constrictions but without damaging the ordered structure of SBA-15. Small-angle X-ray diffraction (XRD) analysis provided additional evidence for the presence of these oxides in the ordered mesopores after thermal treatment below 300 °C and for the diffusion of these species to the external surface of SBA-15 after calcination above 600 °C. Changes in the Al coordination in these oxides with an increase in the temperature of calcination were monitored by Al^{27} MAS NMR, showing the existence of surface, framework, and oxygen-deficient Al^{3+} sites. After consecutive depositions, the resulting composites were calcined at higher temperatures (600−800 °C) and characterized by wide-angle powder XRD, which revealed the existence of nanoparticles of double and single oxide phases formed in the aforementioned temperature range. The crystallite size of these nanoparticles estimated using the Scherrer formula were, in general, larger than the silica pore widths, suggesting the surface diffusion of these oxides and sintering of small nanoparticles during thermal treatment.

KEYWORDS: sol−gel synthesis • mixed-metal oxides • nitrogen adsorption • oxide deposition • SBA-15

INTRODUCTION

The synthesis and characterization of M41S-type molecular sieves (1), such as MCM-41 and MCM-48, is considered to be a major breakthrough in materials science. Further progress in the synthesis of materials with ordered, uniform, and accessible mesopores, especially silica-based materials, has been accelerated by the use of triblock copolymers as soft templates (2, 3). Among ordered mesoporous silicas (OMSs) such as SBA-15, SBA-16 (2), and FDU-1 (3), the former has been the most extensively studied. The popularity of SBA-15 is due to the possibility of synthesizing this material under various experimental conditions. Furthermore, SBA-15 exhibits a 2D hexagonal arrangement of cylindrical mesopores (*P6mm* symmetry) of larger size, thicker pore walls, and higher hydrothermal stability (4) in comparison to its analogue MCM-41, which is a cationic surfactant-templated OMS. Also, the polymer used for the synthesis of SBA-15, poly(ethylene oxide)−poly(propylene oxide)−poly(ethylene oxide) (PEO−PPO−PEO), is biodegradable and cheaper than the alkylammonium surfactants employed in the synthesis of MCM-41. Another important property of SBA-15 is the presence of complementary pores interconnecting hexagonally ordered mesopores (5, 6). This feature makes SBA-15 an attractive material for catalysis because the aforementioned complementary porosity creates a 3D system of pores, which facilitates diffusion inside the entire structure. These fine interconnecting pores were essential for usage of SBA-15 as a hard template for the synthesis of mesoporous carbons, polymers, and inorganic and composite materials. After the pores of silica are filled with suitable precursors and the template is dissolved, a stable 3D inverse replica of SBA-15 can be obtained. This synthesis strategy has been used for the preparation of carbons (7), noble metals (8), and single (9−12) and mixed-metal oxides (13−16).

To overcome major drawbacks of hard-templating and of the cocondensation synthesis of purely inorganic ordered mesoporous materials, extraframework postsynthesis grafting appears to be an attractive option. This synthesis route also opens new possibilities for the selection of the best conditions for each particular material to be grafted in the form of films or particles within the pores of the OMS substrates and for the exploration of phases that can only

be obtained by sol–gel chemistry. For instance, SBA-15 with single Fe[III] sites (17) and TiO$_2$ films (18) were prepared by nonhydrolytic sol–gel methods involving alkoxide precursors through condensation with silanol groups present on the silica surface. Using similar sol–gel procedures, thin layers and small nanoparticles of TiO$_2$, ZrO$_2$, MoO$_3$, WO$_3$, and NiO were also incorporated into SBA-15 (19). Also, mixtures of oxides such as NiMo–SBA-15 (20) and copper oxide deposited on CeO$_2$ (21) were reported. Small particles of titanium and zirconium oxides were prepared by chemical decomposition of precursor solutions or their hydrolysis in the presence of SBA-15 (22). Other nanoparticles such as LaCoO$_3$ were also generated in situ using microwave conditions (23). Nevertheless, only a limited number of inorganic oxides–SBA-15 nanocomposites have been prepared by sol–gel methods known to yield mixed-metal oxides (24–31) in a single impregnation step. Another important issue, the thermal stability of mixed oxide coatings on OMSs such as SBA-15, has not been investigated yet.

Homogeneously mixed oxides prepared by sol–gel show in many cases higher acidity and, consequently, better catalytic activity in comparison to most single oxide systems (32–36). In general, the mixing of distinct oxide phases, especially those containing metal cations at different oxidation states, results in the formation of surface and lattice defects and, consequently, catalytically active sites (32–36). These sites can possess acidic and/or basic properties. While the latter are associated with O^{2-} vacancies (37, 38), the former are usually related to exposed metal cations (Lewis sites) bridged by surface hydroxyls and to electron-deficient hydroxyl groups bound to transition metals (Brönsted sites) (34, 35, 38). Also, the double and mixed oxide materials of Al^{3+}, Ti^{4+}, Zr^{4+}, and Ni^{2+} oxides are largely abundant, attractive for catalytic (39, 40), sensing (31), and optical applications (41, 42), and potentially useful for the fabrication of electronic materials (43–46) and novel nanostructures (47–49). The aforementioned properties are affected not only by chemical composition but also by nanoarchitecture, such as thin films and nanoparticles (50). Thus, the development of simple and environmentally friendly synthetic routes for oxides, as well as of efficient methods to characterize these oxide materials, is extremely important.

In the present work, the formation of thin films and of nanoparticles containing two transition-metal oxides on the walls of ordered mesopores of the template-free SBA-15 via the condensation of metal alkoxides of Al, Ti, and Zr and of an alcoholic solution of Ni(NO$_3$)$_2$ · 6H$_2$O is studied. An inorganic acid was used as a catalyst to promote the further condensation and grafting of alkoxide species on mesoporous silica surfaces followed by low-temperature thermal treatments. The process of deposition was repeated until the silica pores were highly loaded with metal oxides. The adsorption and structural properties of these new nanocomposite materials were investigated using thermogravimetric analysis (TGA), nitrogen adsorption at −196 °C, small- and wide-angle powder X-ray diffraction (XRD), and Al magic angle spinning (MAS) NMR spectroscopy.

Nitrogen adsorption showed that the oxide layers formed on the silica surfaces after one or two impregnations (depositions) were quite homogeneous, whereas pore constrictions were observed after three or four impregnations and thermal treatments at 300–600 °C. These observations agree with an "island-type" formation (51) of thin films. Evidence for the incorporation of oxide films within the ordered mesopores was provided by a recently proposed method to estimate the pore widths of silica MCM-41 and SBA-15 materials using small-angle X-ray scattering (SAXS) (52). According to this method, the pore widths of OMSs with *P6mm* symmetry can be evaluated using the relative intensities of the diffraction peaks in the SAXS patterns. Qualitatively, larger or lower ratios found for the present nanocomposites as compared to the SBA-15 treated at the same temperatures provided evidence for the presence of oxides within or outside the silica mesopores, respectively. The NMR spectra revealed that for the Al-containing materials the thermal treatment temperature promoted considerable changes in the Al^{3+} environments (53). These materials possessed octahedral and tetrahedral sites (54) after treatment at a lower temperature of 300 °C, whereas pentahedral sites and signal attenuation (53, 55, 56) were found after treatment of these samples at 600 °C. Also, after several depositions and calcinations above 600 °C, crystalline phases of ZrTiO$_4$ and NiTiO$_3$ and of nanoparticles of various single oxide phases were obtained. The size of the aforementioned crystalline nanoparticles was, in general, larger than that of the silica pores, highlighting the surface diffusion and sintering (51, 57, 58) of the various oxide species present. Therefore, this work is beneficial for the preparation of silica-supported metal oxide mesostructures, which are of great interest for adsorption, catalysis, and related applications.

EXPERIMENTAL SECTION

Synthesis of SBA-15. The SBA-15 materials were prepared according to the procedure reported by Zhao et al. (2) but using a short-time synthesis for the first step of the self-assembly reaction. Tetraethyl orthosilicate (TEOS; Fluka) was used as the silica source and EO$_{20}$–PO$_{70}$–EO$_{20}$ (P123; Pluronic 123 from BASF) polymer as the structure-directing agent. In a typical synthesis, 4.00 g of P123 was added to 144 mL of an aqueous solution of 1.7 M hydrochloric acid (HCl), and the resulting solution was stirred for 4 h at 40 °C. Next, TEOS was added dropwise at the mass ratio of TEOS/P123 = 2, and the mixture was stirred for 2 h. The synthesis gel was transferred to Teflon-lined sealed containers and kept at 100 °C for 48 h under static conditions. The final product was filtered, washed with water, and dried for 12 h at 80 °C. The as-synthesized samples were solvent-extracted using 4 mL of a concentrated HCl solution and 200 mL of ethanol (95 %) per 1 g of the as-prepared material. This procedure was performed twice at 80 °C, and after each extraction, the sample was filtered, washed with ethanol and water, and dried. This template-free sample was labeled as SBA-15SE. For a better comparison with the composite materials obtained at different calcination temperatures, different parts of this solvent-extracted sample were calcined at 300 and 600 °C and labeled as SBA-15* and SBA-15**, respectively.

Synthesis of Mixed-Metal Oxides–SBA-15 Composites. The deposition of mixed-metal oxides was performed by the condensation of suitable precursors in the mesopores of SBA-15; these precursors were generated prior to the impregnation

process. In a typical synthesis, 30 mL of isopropyl alcohol (Acrós Organics) solutions of 0.01 M Ti(O^{i}Pr)$_4$ (Acrós Organics) and 0.01 M Zr(OPr)$_4$ (Aldrich), 0.01 M Ti(O^{i}Pr)$_4$ and 0.02 M Al(O^{i}Pr)$_3$ (Aldrich), or 0.01 M Zr(OPr)$_4$ and 0.02 M Al(O^{i}Pr)$_3$ was reacted for 2 h at room temperature. For the Ni^{2+}-containing materials, Ni(NO$_3$)$_2$.6H$_2$O (Acrós Organics) was dissolved in 30 mL of isopropyl alcohol to obtain a 0.10 M solution of this salt. After 1 h of stirring, these solutions were transferred to an oven at 80 °C and kept under static conditions in sealed containers for 12 h. For all of the Al-containing materials, ~0.1 mL of HCl was initially added to help dissolve any aluminum(3+) oxoalkoxides, or other oligomeric species formed (25). After dissolution, 1.00 mL of acrylonitrile (Aldrich) was added to the isopropyl alcohol solution as a coordinating solvent to chloroalkoxo species. Next, 0.250 g of dry SBA-15 was added to all of these precursor solutions, and the resulting mixtures were vigorously stirred for several hours, followed by the addition of 0.1 mL of concentrated HCl. The gels were immediately transferred to an oven in open containers and slowly dried under static conditions at 80 °C. These samples were later quickly washed, filtered with isopropyl alcohol, ethanol, and water, and finally dried at 80 °C for 12 h. The as-synthesized nanocomposite materials were calcined in a horizontal quartz tube oven at 300 °C under flowing air for 2 h and a heating rate of 10 °C min^{-1}. Approximately 80 wt % of these calcined samples was then added to the same amounts of precursor solutions, and all procedures were repeated three or four times. For the latter materials, consecutive calcinations were performed at 600 °C using a 10 °C min^{-1} heating rate under flowing air; the samples were kept for 2 h at the final temperature. The samples calcined at 300 °C were labeled as nM$_1$M$_2$−SBA-15*, and those calcined at 600 °C were denoted as nM$_1$M$_2$−SBA-15**, where n indicates the number of impregnation steps and M$_1$ and M$_2$ denote the metal species present in the silica framework. Calcination at higher temperatures (700 and 800 °C) was also used to induce crystallization in these materials for powder XRD analysis.

Characterization. The samples were analyzed by nitrogen adsorption, low- and wide-angle powder XRD, Al^{27} MAS NMR spectroscopy, and thermogravimetry.

Nitrogen adsorption isotherms were measured at −196 °C using ASAP 2010 and 2020 volumetric adsorption analyzers manufactured by Micromeritics (Norcross, GA). Before the adsorption measurements, the template-free SBA-15 and calcined nanocomposites were outgassed under vacuum at 200 °C for at least 2 h. The specific surface area was determined by the standard Brunauer−Emmett−Teller (BET) method in the relative pressure range of 0.05−0.2. The pore size was evaluated using the Barrett−Joyner−Halenda method calibrated for cylindrical pores according to the improved Kruk−Jaroniec−Sayari (KJS) method (59).

The XRD analyses were conducted for the calcined samples using a PANanalytical, Inc., X'Pert Pro multipurpose diffractometer (MPD) with Cu Kα radiation (1.5406 Å), with an operating voltage of 40 kV, 0.020° step size, 3 s step time, and 10.0° < 2θ < 80.0° at room temperature. The small-angle XRD of the template-free SBA-15 and composites were measured using the same conditions except a 20 s step time and 0.400° < 2θ < 5.000°. The size of crystallites, D, was calculated using Scherrer's formula $D = 0.9\lambda/(\beta \cos \theta)$, where 0.9 is the shape factor, λ is 0.154 nm, β is the full width at half-height, and θ is the diffraction angle for a particular crystalline phase.

The Al^{27} MAS NMR spectra were recorded using a Bruker DMX-400WB spectrometer (Bruker Instruments, San Jose, CA) operating at 9.4 T and XWINNMR software operating in a UNIX environment on a Silicon Graphics computer. The single-pulse experiments (18° pulse) were performed using a resonance frequency of 100 MHz and spinning frequencies in the range of 5−10 MHz.
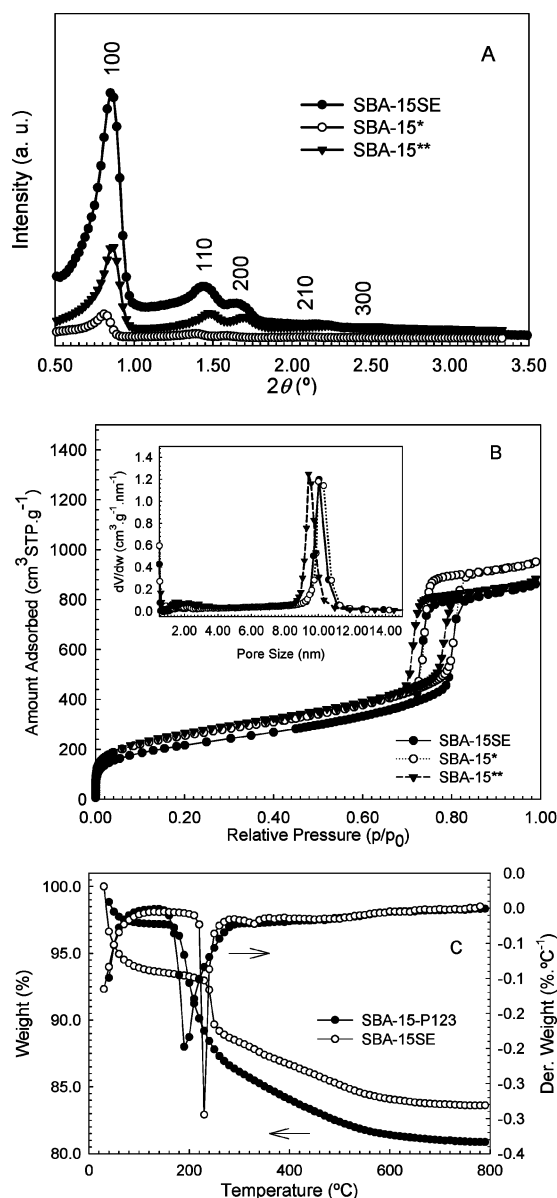

FIGURE 1. (A) Small-angle XRD data and (B) nitrogen adsorption isotherms at −196 °C with the corresponding PSD (inset) curves for the template-free SBA-15 and materials obtained at different calcination temperatures. The PSD curves were obtained using the improved KJS method reported in ref 59. (C) TGA curves for the SBA-15-P123 as-prepared nanocomposite and SBA-15SE.

The TGA measurements were performed on a TA Instruments TGA 2950 thermogravimetric analyzer using a high-resolution mode. The curves were recorded in flowing air with a heating rate of 10 °C min^{-1} up to 800 °C.

RESULTS

Characterization of the SBA-15 Materials. The small-angle XRD patterns recorded for the template-free SBA-15 samples (Figure 1A) show up to five diffraction peaks, which were assigned according to the $P6mm$ symmetry group (see Table 1S in the Supporting Information). The average unit cell parameters $\bar{a}$, shown in Table 1, decreased from 12.15 for SBA-15SE to 11.52 nm for SBA-15** because of shrinkage of the nanostructure during calcination at 600 °C, whereas no considerable difference

Table 1. Adsorption and Small-Angle XRD Data Obtained for the SBA-15 Samples and Composites Obtained after One and Two Impregnations and Thermally Treated at 300 and 600 °C[a]

sample	$\bar{a}$ [nm]	I_{110}/I_{200}	w_{KJS} [nm]	b [nm]
SBA-15SE	12.15	1.7	10.03	2.12
SBA-15*	12.09	1.6	10.00	2.09
SBA-15**	11.52	1.3	9.41	2.11
1NiAl−SBA-15*	12.07	1.6	9.68	2.39
2NiAl−SBA-15*	12.18	1.6	9.46	2.72
1NiAl−SBA-15**	11.84	1.5	9.34	2.50
2NiAl−SBA-15**	11.75	1.5	8.98	2.77
1NiTi−SBA-15*	11.99	1.4	9.27	2.72
2NiTi−SBA-15*	12.09	1.5	8.99	3.10
1NiTi−SBA-15**	11.75	1.2	9.12	2.63
2NiTi−SBA-15**	11.75	1.2	8.82	2.93
1NiZr−SBA-15*	12.03	1.5	9.73	2.30
2NiZr−SBA-15*	12.17	1.7	9.31	2.86
1NiZr-SBA-15**	11.60	1.5	9.26	2.34
2NiZr−SBA-15**	11.62	1.4	8.98	2.64
1ZrTi−SBA-15*	12.09	1.6	9.51	2.58
2ZrTi−SBA-15*	12.12	1.2	8.75	3.37
1ZrTi−SBA-15**	11.79	2.0	9.25	2.54
2ZrTi−SBA-15**	11.50	0.9	8.44	3.06
1AlZr−SBA-15*	12.06	1.4	9.35	2.71
2AlZr−SBA-15*	11.42	1.5	8.53	2.89
1AlZr−SBA-15**	11.41	1.4	9.06	2.35
2AlZr−SBA-15**	11.26	0.9	8.09	3.17
1TiAl−SBA-15*	12.00	1.5	9.83	2.17
2TiAl−SBA-15*	11.39	1.9	9.11	2.28
1TiAl−SBA-15**	11.74	1.6	9.12	2.62
2TiAl−SBA-15**	11.58	1.4	9.03	2.55

[a] $\bar{a}$ = average unit cell parameter obtained neglecting the (100) peak or any other reflection that differed greatly in a (see Tables 1S−3S in the Supporting Information); I_{110}/I_{200} = relative intensity corresponding to the (110) and (200) diffraction planes, respectively; w_{KJS} = pore width calculated from the nitrogen adsorption isotherms at −196 °C using the equation reported in ref 59; b = pore wall thickness calculated as $b = \bar{a} - w_{KJS}$.

was observed between the $\bar{a}$ values for SBA-15SE and SBA-15*. The observed differences in the values of $\bar{a}$ found for these materials were accompanied by pronounced changes in the intensities ratios for the 110 and 200 reflections (52) (see Table 1), which decreased from 1.7 for SBA-15SE to 1.3 for SBA-15**.

This intensity ratio was recently used to determine the pore width of materials with *P6mm* symmetry using SAXS (52). Not only the diffraction angles but also the intensities of the (100) and (200) reflections are sensitive to the changes in the pore widths. Because the exact determination of the (100) peak position is not always a simple task, the (200) peak was used instead of (100). Also, absolute intensities are subjected to errors; thus, the relative intensities are preferred, whereas the (110) peak is used as a reference.

Nitrogen adsorption isotherms measured at −196 °C (Figure 1B) are of type IV, with the characteristic hysteresis loop of the materials having large cylindrical mesopores. The steepness of the capillary condensation steps on the adsorption isotherms for these materials also evidences the uniformity of these mesopores. The calculated specific surface area for these samples increased from 784 m² g⁻¹ for SBA-15SE to 968 m² g⁻¹ for SBA-15** (see Table 2S in the Supporting Information). Note that the lower surface area for the sample SBA-15SE may result from the trace amounts of polymer retained in the structure, which can cause a partial blocking of the micropores. The aforementioned parameters are summarized in Table 2S (Supporting Information).

The pore-size distribution (PSD) curves (inset in Figure 1B) were calculated using the improved KJS method. The pore width (see Table 1) was ∼10.0 nm for SBA-15SE and SBA-15*, whereas for SBA-15**, this value was ∼9.5 nm. The reduction in the pore width for this material agreed with the calculated average unit cell parameter, $\bar{a}$, and with the relative intensity of the 100 and 200 reflection peaks, I_{110}/I_{200}, obtained from the small-angle XRD patterns (52). Meanwhile, the pore wall thicknesses, b, of these samples were very similar, ∼2.1 nm.

Integration of the PSD curves in the range from 1 to 16 nm for the samples studied gave the pore volumes (see Table 2S in the Supporting Information), which are in satisfactory agreement with the single-point pore volumes obtained from adsorption isotherms at a relative pressure of 0.98. The volumes of complementary pores were calculated by integration of the PSD curves between 1 and 3 nm. These values increased considerably with increasing calcination temperature, up to 0.13 cm³ g⁻¹ in comparison to 0.04 cm³ g⁻¹ obtained for the SBA-15SE material. This trend follows the change in the BET surface area for these materials; larger surface areas were obtained for the materials with higher complementary porosities.

The TGA profile of the as-prepared SBA-15 (Figure 1C) indicates a total weight loss of ∼19%. About 3% of this weight loss (observed below 150 °C) corresponds to the desorption of water, and the remaining weight loss (∼16%) refers to the polymer template, P123, as well as to the condensation of silanol groups present on the silica surface. In general, weight losses of ∼40−50% are observed for the SBA-15 samples, which are not thoroughly washed after synthesis. The observed ∼19% weight loss indicates that at least 50% of the polymer was removed during the initial washing of the as-synthesized SBA-15 sample. However, the TGA curve for the extracted SBA-15 sample shows ∼6% weight loss below 150 °C, whereas the remaining weight loss accounts for ∼60% of that observed for the as-prepared material. The presence of polymer within small complementary pores makes the surface of SBA-15 more hydrophobic, which is reflected by a smaller amount of adsorbed water and, consequently, by a smaller weight loss below 150 °C. Also, the presence of a residual amount of the polymer template after extraction was found to protect both the
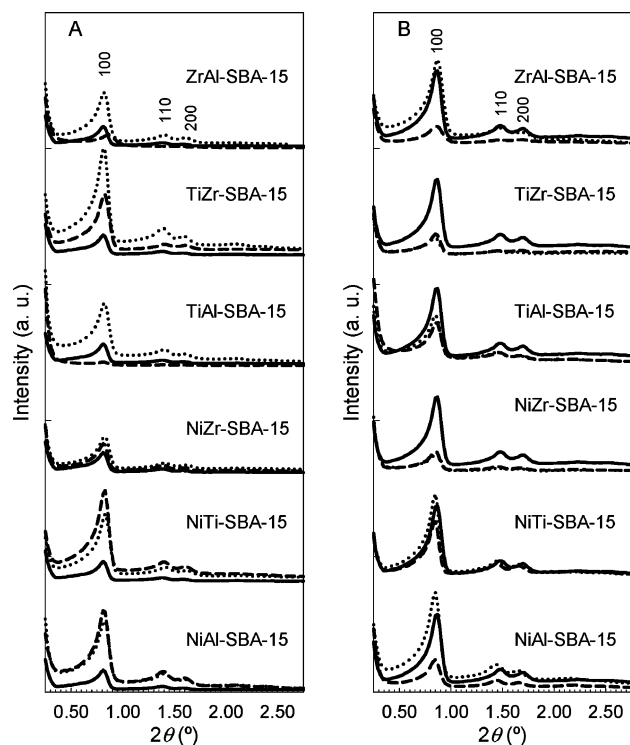
ARTICLE

FIGURE 2. Small-angle XRD patterns for the materials obtained at 300 °C (A) and 600 °C (B). The patterns for the SBA-15* and SBA-15** samples are represented by solid lines. The composite samples prepared after one and two impregnations are represented by dotted and dashed lines, respectively. The peaks were characteristic of the *P6mm* symmetry, and at least three diffraction peaks were identified as (100), (110), and (200); their specifications are listed in Tables 2S–4S in the Supporting Information.

ordered mesopores and complementary pores against shrinkage or collapse during calcination (60).

XRD and Al^{27} MAS NMR Studies of the Mixed Oxide–SBA-15 Nanocomposites.

The small-angle XRD spectra, shown in Figure 2 for the SBA-15 samples and nanocomposites obtained after one or two casting cycles and calcinations at 300 °C (A) and 600 °C (B), were also assigned according to the *P6mm* symmetry group (see Tables 3S and 4S in the Supporting Information), the same group as that assigned for unmodified SBA-15 samples. Calcination of the samples at higher temperature (600 °C) caused a shift of the XRD reflections toward larger 2θ values because of structure shrinkage. Also, the calculated d spacing and average unit cell parameters $\bar{a}$, shown in Tables 3S and 4S in the Supporting Information and Table 1, decreased for the samples obtained at 300 and 600 °C. These values are similar to those of SBA-15 calcined at the same temperature. For calculation of $\bar{a}$, the (100) reflection was not included because of difficulty in determining the exact position of this reflection. Nevertheless, while $\bar{a}$ was ~12.0 nm for samples calcined at 300 °C, for the ones obtained at 600 °C, the unit cell values were below 11.8 nm. In addition to the aforementioned parameters, the relative intensities of the (110) and (200) peaks were calculated and compared to those of unmodified SBA-15 samples. For the nanocomposites studied, the direct calculation of the pore width by this method is not possible without implementing the necessary correc-

tions by using reference samples containing these oxides. Nevertheless, a qualitative approach was used to determine whether the surface of these nanocomposites resembles that of the initial silica, or metal oxides if a homogeneous layer of the latter was formed on the siliceous pore walls, leading to a small reduction in the pore widths. In the latter case, the deposition of these metal oxides onto the siliceous pore walls should enlarge the aforementioned relative intensity in comparison to the value obtained for unmodified SBA-15 samples. Because the pore width of SBA-15** was ~9.4 nm, which is similar to those obtained for the nanocomposites studied, this SBA-15 sample was used as a reference.

On the basis of the values of the aforementioned relative intensity (Table 1), some metal oxides–SBA-15 composite samples were found to exhibit lower ratios than 1.3, which was obtained for the unmodified SBA-15** sample. Namely, the lower value is observed for 2ZrTi–SBA-15 after calcination at 300 °C and for four other composites that were calcined at 600 °C. The lowest intensity ratios (~0.9) are for the 2ZrTi–SBA-15** and 2AlZr–SBA-15** samples. Note that, for 1ZrTi–SBA-15**, this relative intensity is larger (~2.0) than that for the material after two impregnations. More consistent values are observed for the NiAl–, NiZr–, and TiAl–SBA-15 systems, with intensity ratios in the range of ~1.4–1.9. In the case of the NiTi–SBA-15 materials, the relative intensity for the samples calcined at 600 °C was below that for SBA-15**, and for the samples treated at 300 °C, it was above the value for unmodified silica. These results suggest that considerable changes occurred on the surface of ordered mesopores during thermal treatment of these nanocomposites.

In addition to the aforementioned XRD data, the Al^{27} MAS NMR spectra (Figure 1S in the Supporting Information) recorded for some of the Al-containing materials revealed the presence of distinct sites for the samples calcined at different temperatures (53). For the 1TiAl–SBA-15* and 1TiAl–SBA-15** samples, octahedral (AlO$_6$) and tetrahedral (AlO$_4$) sites at chemical shifts of ~0–3 and ~56 ppm were detected (53–56), respectively (Figure 1SA in the Supporting Information). The same was observed for 2TiAl–SBA-15**, whereas after calcination at 600 °C, both peaks were largely attenuated. For the 1AlZr–SBA-15* sample (Figure 1SB in the Supporting Information], octahedral and tetrahedral Al sites were also detected, with an additional pentahedral site (AlO$_5$) at ~30–45 ppm. The spectrum for this sample shows a high signal-to-noise ratio, which is reduced considerably for 1AlZr–SBA-15**. The treatment of Al-containing siliceous materials at higher temperatures was found to decrease the intensities of the peaks corresponding to the AlO$_6$ and AlO$_4$ units and the appearance of the AlO$_5$ peak (~30–45 ppm) (53–56). Also, for Al-modified MCM-41 by postsynthesis grafting, only the AlO$_4$ and AlO$_6$ sites were identified, even after calcination at 550 °C (61).

Furthermore, all nanocomposites were characterized by wide-angle powder XRD, and the corresponding patterns are shown in Figure 3 for the ZrTi–SBA-15 (A) and TiAl–SBA-15 (B) materials and in Figure 2S and Table 5S (Supporting
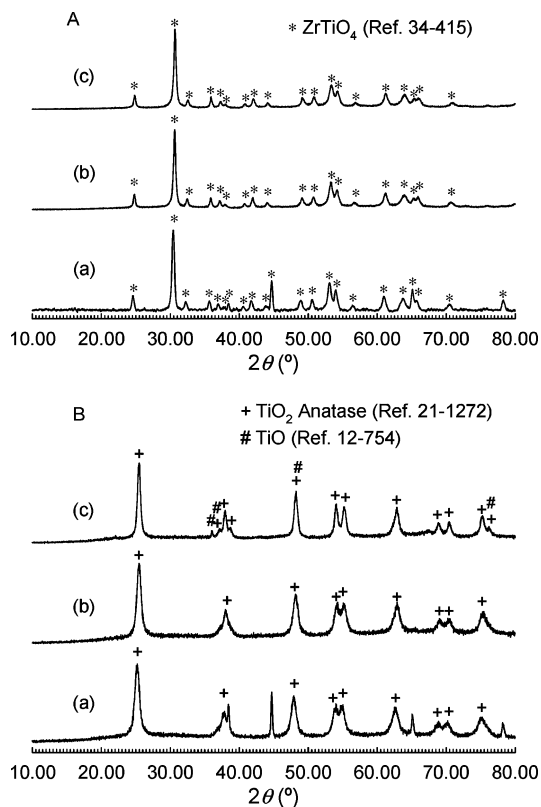
FIGURE 3. Wide-angle powder XRD patterns of the 3ZrTi—SBA-15 and 3TiAl—SBA-15 metal oxides—SBA-15 nanocomposites after three impregnations, followed by calcination at 600 °C (a), 700 °C (b), and 800 °C (c) for 2 h under an air atmosphere. These patterns were shifted in increments of 125 in the relative intensity axis (percent scale) for better presentation of the data. For the assignments and additional information on the crystalline phases identified, see Table 5S and Figure 2S in the Supporting Information.

Information) for all remaining materials. Only the materials obtained after three or four impregnation cycles at temperatures above 600 °C presented crystalline oxide phases. For the NiAl—SBA-15 nanocomposites, only the NiO phase was identified after calcination at 600 °C. The presence of Al_2O_3 was evident after thermal treatment of this material above 700 °C, without detection of a double oxide phase. These results are in agreement with data reported for an analogous system prepared by the coprecipitation of metal salts (62), while a double oxide phase (spinel) was reported for a sample obtained by the sol—gel route but in the presence of propylene oxide (26). For the NiZr—SBA-15 system, ZrO_2 was identified at 600 °C, while NiO was detected after baking at higher temperatures. In the case of the NiTi—SBA-15 nanocomposites, the double oxide phase $NiTiO_3$ was obtained for all three calcination temperatures. For the samples obtained at 600 and 700 °C, TiO_2 anatase was also present. At a temperature of 700 °C, the rutile phase began to form, and this was the single polymorphic phase of TiO_2 present with $NiTiO_3$ after calcination at 800 °C. Peaks characteristic of SiO_2 (cristobalite) were also present for the latter composite.

For the materials obtained from two metal alkoxides, the double oxide phase of $ZrTiO_4$ was the single phase detected for the 3ZrTi—SBA-15 nanocomposites (see Figure 3A). The

3TiAl—SBA-15 sample (Figure 3B) shows TiO_2 anatase as the single phase after calcinations at 600 and 700 °C, above which TiO was also identified, whereas previous reports revealed the formation of Al_2TiO_5 with TiO_2 for aluminum and titanium oxide systems (31, 48). The crystalline phases present in the AlZr—SBA-15 nanocomposite after calcination up to 800 °C could not be assigned.

The crystallite sizes for the identified phases were calculated according to Scherrer's formula (Table 6S in the Supporting Information). They were found to be larger than the silica pores, in most cases larger than 9 nm after calcination at 600 °C. For 4NiAl—SBA-15, Al_2O_3 nanocrystals of approximately 9 nm were obtained. Also NiO nanoparticles of ~9 and 14 nm were found in 4NiZr—SBA-15 calcined at 700 and 800 °C, respectively. For the latter, ZrO_2 nanoparticles in the range of 14—25 nm were formed in the range of 600—800 °C. Note that, for the same nanocomposite, the crystallite size of each identified oxide phase was often different. For instance, the smallest nanoparticles were for the Al_2O_3 phase and the largest for NiO in the NiAl—SBA-15 materials, whereas aluminum oxide was amorphous in the presence of TiO_2 nanocrystals.

Adsorption Studies of the SBA-15 Nanocomposites. Nitrogen adsorption isotherms at −196 °C were measured for the SBA-15 nanocomposites obtained after calcination at 300 and 600 °C. The adsorption isotherms for the former materials are shown in Figure 4A, for the samples containing nickel, and in Figure 4B, for the Al-containing samples. As can be seen from parts A and B of Figure 4, the adsorption isotherm curves are of type IV, showing that the structure of SBA-15 is preserved after each impregnation cycle. Furthermore, small shifts to lower relative pressures in the capillary condensation steps are observed for successive impregnations, suggesting a decrease in the width of the pores. The capillary condensation steps remain steep after the first impregnation, as would be expected for the formation of a quite homogeneous layer of these oxides on the silica surface. In general, for the second and concomitant impregnations of oxide species, a continuous broadening of the condensation steps and hysteresis loops is observed. This behavior is more pronounced for the 3NiZr—SBA-15 and 2AlZr—SBA-15 samples calcined at 300 °C because of the formation of less uniform layers. The isotherm curve for 3NiTi—SBA-15 shows even a second desorption step, suggesting some pore constrictions. Furthermore, these changes are accompanied by a large reduction in the total pore volume of these composite samples (see Table 7S in the Supporting Information). Because the physical properties of these nanocomposite materials greatly differ from those of unmodified SBA-15, the specific pore volumes per gram of the samples are less informative and suitable corrections based on the densities of these mixed oxides would be desirable, as was done for silicon carbide modified OMSs (63). Such normalization is difficult to make because the phases of each oxide component are unknown at the early stages of deposition. However, it is quite clear that after several impregnations (three or four impregnations) these
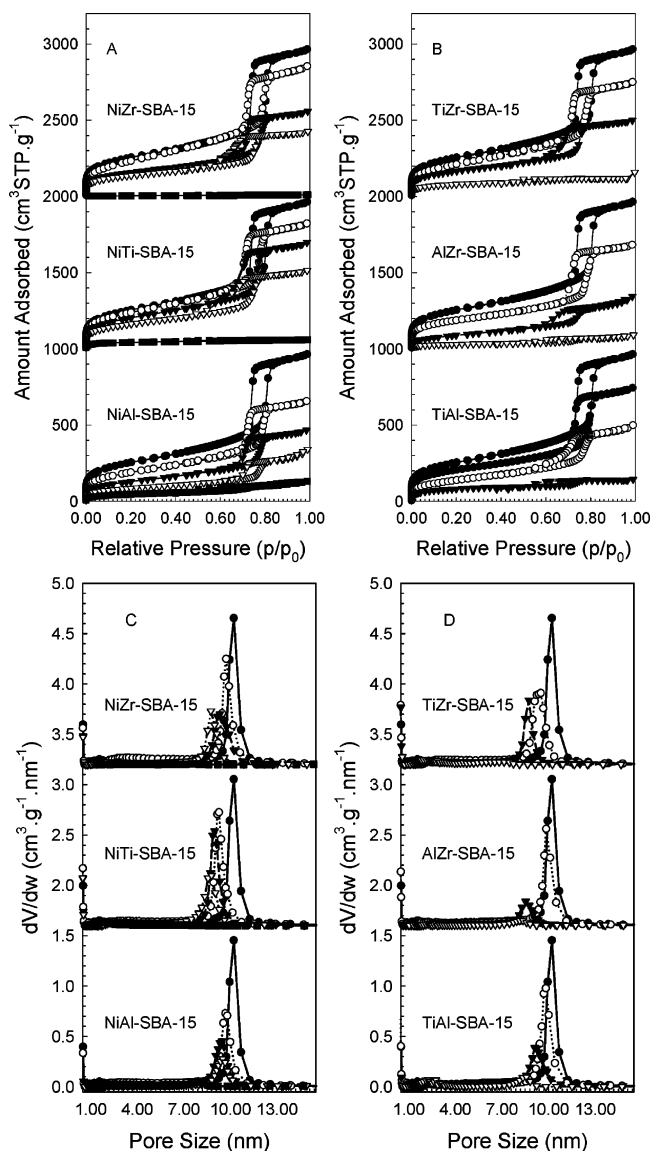
FIGURE 4. Nitrogen adsorption isotherms at −196 °C (A and B) and the corresponding PSD curves (C and D) for various metal oxides−SBA-15 nanocomposite materials calcined at 300 °C in comparison to SBA-15SE. In all figures, the curves with solid dots are for SBA-15SE, those with open dots refer to the samples after the first impregnation, those with solid triangles refer to the samples after the second impregnation, and those with open triangles and squares were used to denote the samples after the third and fourth impregnations, respectively. The PSD curves were obtained using the improved KJS method reported in ref 59.

results provide information that the accessibility to the mesopores was significantly reduced. For the final nanocomposites (see Figure 3S in the Supporting Information), the presence of broad adsorption steps and broad hysteresis loops indicates the formation of constrictions within ordered mesopores. Such constrictions would result in small particles formed on the surface of initial deposits.

As illustrated in parts C and D of Figure 4, the calculated PSD curves show a decrease in the pore size for the consecutive impregnations, similar to the shifts in the relative pressures of the condensation steps (see the adsorption isotherms). After three depositions of mixed-metal alkoxides and four depositions of the Ni-containing materials, the pore

size decreased from ∼10 nm for the SBA-15SE materials to ∼8 nm for these samples. Only the 4NiTi−SBA15* and 3ZrTi−SBA-15* samples exhibited broad distributions with maxima below 2 nm. For the samples prepared after three or four impregnations, the reduction in the mesopore widths compared to the increase in the amount of pores of smaller widths suggests irregular filling of the mesopores.

For the nanocomposites after one or two impregnations prepared at 600 °C, the adsorption isotherms are also of type IV. The condensation steps are, in general, steeper for the materials obtained after one impregnation with metal oxides. Also, in comparison to the same samples prepared at 300 °C, further shifts to lower relative pressures in the condensation steps were observed for the former because of possible structure shrinkage. The most noticeable changes are visible on the desorption branches, e.g., broad hysteresis for 2AlZr−SBA-15** (see Figure 3Se in the Supporting Information). Nevertheless, the PSD curves for the aforementioned materials show that the pores of both 2AlZr−SBA-15* and 2AlZr−SBA-15** (Figure 3Sf in the Supporting Information) are quite uniform. Furthermore, the PSD curves reveal that the pore widths for these nanocomposites decreased with increasing number of impregnations and increasing calcination temperature (see Table 1).

The pore wall thicknesses (Table 1) were estimated for the samples prepared after two impregnations calcined at 300 and 600 °C. This parameter was larger for the composites than for unmodified SBA-15 samples. With the exception of the Al-containing materials, the samples obtained at 300 °C were found to have thicker pore walls than those obtained at 600 °C after the same number of impregnations. This effect of the calcination temperature on the pore wall thickness was more pronounced for the samples obtained after two impregnations. For the latter, after calcination at 600 °C, thinning of the pore walls was observed; e.g., see data for 2NiTi−SBA-15**, 2NiZr−SBA-15**, and 2ZrTi−SBA-15**.

The specific surface area of the nanocomposites obtained at 300 °C (Table 5S in the Supporting Information) decreased after each impregnation. For instance, in the case of NiTi−SBA-15*, this decrease was ∼6% after the first deposition in comparison to SBA-15*, whereas after two consecutive depositions, this reduction was ∼20%. The third and fourth depositions of oxides resulted in the retention of only ∼64 and 14% of the initial surface, respectively. On average, the first deposition of mixed oxide phases resulted in a ∼16% reduction of the surface area, whereas the average decrease after the second deposition was ∼42% for all materials. For the nanocomposites calcined at 600 °C, some distinct features were observed. While no significant change was observed for 2TiAl−SBA-15**, the surface area increased to ∼50 and 100 m^2 g^{-1} for 2AlZr−SBA-15** and 2NiAl−SBA-15**, respectively, as compared to the same samples prepared at 300 °C. Overall, the surface areas for the nanocomposites prepared at 600 °C were lower than those for the samples calcined at 300 °C.

DISCUSSION

The results obtained from nitrogen adsorption isotherms at −196 °C show that for the silica-metal oxides nanocomposites obtained after one or two depositions and calcinations at 300 °C showed quite uniform oxide coatings. Furthermore, the pore widths for these materials were smaller than those of unmodified SBA-15 samples treated at the same temperatures. Differences in the pore widths were also noticed for the samples calcined at 300 and 600 °C. In both cases, the decrease in the pore width was more pronounced for unmodified SBA-15 samples, highlighting the better thermal stability of the mixed oxides−SBA-15 nanocomposites. After three or four impregnations of oxides, these nanocomposites showed pore constrictions, indicating irregular filling of the pores. After silica dissolution, mostly disordered or even nonporous oxides were obtained, showing the incomplete filling of the pores of SBA-15.

For the materials studied, the metal oxide precursors were initially grafted in a layer fashion, according to the gas adsorption data. After consecutive depositions and thermal treatments at different temperatures, particle growth occurred, which resulted in the formation of constrictions within ordered mesopores. Such constrictions created by irregular nucleation of metal oxides resemble an island-type formation of coatings (51).

A comparison of the relative intensities of the (110) and (200) reflections for the composites prepared after two impregnations shows that the reduction in the coating thickness follows the decrease in I_{110}/I_{200}. Also, the most significant reduction of this thickness was observed for the materials that showed relative intensities below of that of SBA-15**, namely, 2NiTi−SBA-15** and 2TiZr−SBA-15**. Also, the Al^{27} MAS NMR spectra revealed distinct Al sites depending on the calcination temperature and the number of depositions, especially for the AlZr−SBA-15 materials. For the latter, the AlO_5 sites revealed the existence of O-deficient sites (53−55). For the TiAl−SBA-15 samples, the attenuation in the signals of the octahedral (surface) and tetrahedral (framework) sites due to increasing quadrupolar interactions can be seen on the NMR spectra (54, 56). The former samples also showed larger I_{110}/I_{200} ratios and pore wall thickness values after calcination at 300 and 600 °C, as compared to other nanocomposites. Similarly, for the materials containing larger amounts of deposited metal oxides, crystalline phases of single or double oxides were identified after calcination above 300 °C. These results show that, upon crystallization of the aforementioned phases, particles were grown on the external surfaces of SBA-15. For the materials after one or two depositions, this growth is also possible. For instance, the AlO_4 and AlO_5 sites can be formed at the expense of octahedral sites by dehydration of AlOOH or $Al(OH)_3$ surface groups. For higher oxide loadings, an increase in the amount of octahedral Al species can occur with increasing calcination temperature, which can be associated with the formation of bulky Al_2O_3.

Furthermore, the proposed method of analysis of the XRD intensities seems to be sensitive enough to detect changes in the surface properties of these materials studied.

Some oxide-modified SBA-15 materials with narrower pores than the unmodified SBA-15 showed lower I_{110}/I_{200} ratios. The aforementioned analysis of the XRD relative intensities for the nanocomposites studied showed a good correlation with other data, e.g., Al^{27} MAS NMR. A better understanding of the metal oxide deposition within ordered mesopores of SBA-15 is required for the design of oxidation catalysts.

CONCLUSIONS

The adsorption and structural properties of SBA-15 and metal oxides−SBA-15 nanocomposites were investigated by varying loadings of oxides. The formation of metal oxide films and growth of oxide nanoparticles on the internal and external surfaces of ordered mesopores of SBA-15 were successfully probed by nitrogen adsorption and powder XRD at small and wide angles. In particular, the qualitative analysis of small-angle XRD patterns was shown to be a useful tool in detecting small changes in the pore widths of the modified SBA-15 because the silica framework may remain unchanged despite film formation on its surface and shifts in the peak positions cannot be detected. Furthermore, "island-type" deposition of oxide films within cylindrical mesopores of SBA-15 was found. The loading of larger amounts of oxides into mesopores of SBA-15 resulted in their partial blockage and incomplete filling with disconnected particles. Also, the incomplete filling of the fine interconnections present in SBA-15 largely contributed to the collapse of the oxide nanostructure after silica dissolution.

Wide-angle XRD studies of the nanocomposites obtained after several impregnations of metal oxide precursors and calcinations at elevated temperatures revealed single and double oxide nanoparticles in the range of 9−25 nm. After calcination at 800 °C, bulk oxide phases of TiO_2−$NiTiO_3$ were obtained, with particles size above 100 nm. On the basis of the number of deposition cycles and on the diffusion control of each oxide component, mixed oxide thin films and small nanoparticles were coated on the pore walls of SBA-15, or larger crystalline nanoparticles were deposited on the external surface because of the adsorption of complex oligomeric species formed during a partial hydrolytic sol−gel process (25) at a relatively low calcination temperature of ∼600 °C. Somewhat similar findings were reported for Ag-loaded organically modified SBA-15 (64) and for TiO_2-modified SBA-15, for which the presence of films or particles were dependent on the thermal treatment conditions (22). Also, the effect of different loadings of TiO_2 in SBA-15 has been studied, but only changes in the unit cell calculated from small-angle XRD patterns were reported (65). Knowledge about the formation of nanoparticles in ordered mesostructures such as SBA-15 and the effect of thermal treatments on their crystallization and growth is necessary because the catalytic activity of these materials is largely dependent on their surface compositions (17−22, 57, 65−72).

Supporting Information Available: Tables 1S−7S containing small-angle XRD data, adsorption parameters, and powder XRD phase assignments and Figures 1S−3S showing wide-angle powder XRD patterns, additional nitrogen

adsorption isotherms, corresponding PSDs, and ^{27}Al MAS NMR spectra. This material is available free of charge via the Internet at http://pubs.acs.org.

REFERENCES AND NOTES

(1) Beck, J. S.; Vartuli, J. C.; Roth, W. J.; Leonowicz, M. E.; Kresge, C. T.; Schimitt, K. D.; Chu, C. T-W.; Olson, D. H.; Sheppard, E. W.; McCullen, S. B.; Higgins, J. B.; Schlenker, J. L. *J. Am. Chem. Soc.* **1992**, *114*, 10834–10843.

(2) Zhao, D.; Feng, J.; Huo, Q.; Melosh, N.; Fredrickson, G. H.; Chmelka, B. F.; Stucky, G. D. *Science* **1998**, *279*, 548–552.

(3) Yu, C.; Yu, Y.; Zhao, D. *Chem. Commun. (Cambridge)* **2000**, *2000*, 575–576.

(4) Zhang, F.; Yan Yang, H.; Yan Meng, Y.; Yu, C.; Tu, B.; Zhao, D. *J. Phys. Chem. B* **2005**, *109*, 8723–8732.

(5) Kruk, M.; Jaroniec, M.; Ko, C. H.; Ryoo, R. *Chem. Mater.* **2000**, *12*, 1961–1968.

(6) Joo, S. H.; Ryoo, R.; Kruk, M.; Jaroniec, M. *J. Phys. Chem. B* **2002**, *106*, 4640–4646.

(7) Jun, S.; Joo, S. H.; Ryoo, R.; Kruk, M.; Jaroniec, M.; Liu, Z.; Ohsuna, T.; Terasaki, O. *J. Am. Chem. Soc.* **2000**, *122*, 10712–10713.

(8) Han, Y.; Kim, J. M.; Stucky, G. D. *Chem. Mater.* **2000**, *12*, 2068–2069.

(9) Zhu, K.; He, H.; Xie, S.; Zhang, X.; Zhou, W.; Jin, S.; Yue, B. *Chem. Phys. Lett.* **2003**, *377*, 317–321.

(10) Laha, S. C.; Ryoo, R. *Chem. Commun. (Cambridge)* **2003**, *2003*, 2138–2139.

(11) Imperor-Clerc, M.; Bazin, D.; Appay, M.; Beaunier, P.; Davidson, A. *Chem. Mater.* **2004**, *16*, 1813–1821.

(12) Wang, Y.; Xia, Y. *Electrochim. Acta* **2006**, *51*, 3223–3227.

(13) Liu, S.; Yue, B.; Jiao, K.; Zhou, Y.; He, H. *Mater. Lett.* **2006**, *60*, 154–158.

(14) Xiong, L.; Shi, J.; Gu, J.; Li, L.; Huang, W.; Gao, J.; Ruan, M. *J. Phys. Chem. B* **2005**, *109*, 731–735.

(15) Lin, K.; Li, Y. *Nanotechnology* **2006**, *17*, 4048–4052.

(16) Salabaş, E. L.; Rumplecker, A.; Kleitz, F.; Radu, F.; Schüth, F. *Nano Lett.* **2006**, *6*, 2977–2981.

(17) Nozaki, C.; Lugmair, C. G.; Bell, A. T.; Tilley, T. D. *J. Am. Chem. Soc.* **2002**, *124*, 13194–13203.

(18) Yan, W.; Mahurin, S. M.; Overbury, S. H.; Dai, S. *Chem. Mater.* **2005**, *17*, 1923–1925.

(19) Vradman, L.; Landau, M. V.; Kantorovich, D.; Koltypin, Y.; Gedanken, A. *Microporous Mesoporous Mater.* **2005**, *79*, 307–318.

(20) Gutiérrez, O. Y.; Fuentes, G. A.; Salcedo, C.; Klimova, T. *Catal. Today* **2006**, *116*, 485–497.

(21) Shen, W.; Dong, X.; Zhu, Y.; Chen, H.; Shi, J. *Microporous Mesoporous Mater.* **2005**, *85*, 157–162.

(22) Landau, M. V.; Vradman, L.; Wang, X.; Titelman, L. *Microporous Mesoporous Mater.* **2005**, *78*, 117–129.

(23) Yi, N.; Cao, Y.; Su, Y.; Dai, W.; He, H.; Fan, K. *J. Catal.* **2005**, *230*, 249–253.

(24) Bradley, D. C. *Chem. Rev.* **1989**, *89*, 1317–1322.

(25) Bradley, D. C. *Alkoxo and aryloxo derivatives of metals*; Academic Press: San Diego, 2001; p 704

(26) Cui, H.; Zayat, M.; Levy, D. *J. Non-Cryst. Solids* **2005**, *351*, 2102–2106.

(27) Ananta, S.; Tipakontitikul, R.; Tunkasiri, T. *Mater. Lett.* **2003**, *57*, 2637–2642.

(28) Phani, A. R.; Santucci, S. *Thin Solid Films* **2001**, *396*, 1–4.

(29) Andrianainarivelo, M.; Corriu, R. J. P.; Leclercq, D.; Mutin, P. H.; Vioux, A. *J. Sol–Gel Sci. Technol.* **1997**, *8*, 89–93.

(30) Bianco, A.; Paci, M.; Freer, R. *J. Eur. Ceram. Soc.* **1998**, *18*, 1235–1243.

(31) Licoccia, S.; Traversa, E.; Di Vona, M. L. *J. Sol–Gel Sci. Technol.* **2003**, *26*, 119–124.

(32) Tanabe, K.; Sumiyoshi, T.; Shibata, K.; Kiyoura, T.; Kitagawa, J.

(33) Kung, H. H. *J. Solid State Chem.* **1984**, *52*, 191–196.

(34) Busca, G. *Phys. Chem. Chem. Phys.* **1999**, *1*, 723–736.

(35) Busca, G. *Catal. Today* **1998**, *41*, 191–206.

(36) Miller, J. B.; Ko, E. I. *Catal. Today* **1997**, *35*, 269–292.

(37) Lavalley, J. C. *Catal. Today* **1996**, *27*, 377–401.

(38) Davydov, A. A.; Sheppard, N. T. *Molecular spectroscopy of oxide catalyst surfaces*; Wiley: Chichester, U.K., 2003; p 668.

(39) Romanova, R. G.; Petrova, E. V. *Kinet. Catal.* **2006**, *47*, 138–147.

(40) Boschloo, G.; Hagfeldt, A. *J. Phys. Chem. B* **2001**, *105*, 3039–3044.

(41) Dondi, M.; Matteucci, F.; Cruciani, G. *J. Solid State Chem.* **2006**, *179*, 233–246.

(42) Zhang, S.; Zhou, L.; Cheng, J.; Zhang, L.; Zeng, Z. *Mater. Sci. Eng., B* **1997**, *49*, 117–122.

(43) Kurien, S.; Mathew, J.; Sebastian, S.; Potty, S. N.; George, K. C. *Mater. Chem. Phys.* **2006**, *98*, 470–476.

(44) Luo, J.; Xing, X.; Yu, R.; Xing, Q.; Liu, G.; Zhang, D.; Chen, X. *J. Alloys Compd.* **2006**, *420*, 317–321.

(45) Kim, W.; Nam, W.; Kim, S.; Rhee, S. *J. Chem. Eng. Jpn.* **2005**, *38*, 578–587.

(46) Mossi, K.; Bryant, R.; Mane, P. *Integr. Ferroelectr.* **2005**, *71*, 221–232.

(47) Taylor, D. J.; Fleig, P. F.; Page, R. A. *Thin Solid Films* **2002**, *408*, 104–110.

(48) Innocenzi, P.; Martucci, A.; Armelao, L.; Licoccia, S.; Vona, M. L. D.; Traversa, E. *Chem. Mater.* **2000**, *12*, 517–524.

(49) Kim, H.; Kim, H. *J. Nanosci. Nanotechnol.* **2006**, *6*, 505–509.

(50) Shiju, N. R.; Guliants, V. V. *Appl. Catal., A* **2009**, *356*, 1–17.

(51) Tersoff, J.; LeGoues, F. K. *Phys. Rev. Lett.* **1994**, *72*, 3570–3573.

(52) Pikus, S.; Solovyov, L. A.; Kozak, M.; Jaroniec, M. *Appl. Surf. Sci.* **2007**, *253*, 5682–5687.

(53) Okuno, M.; Shimada, Y.; Schmücker, M.; Schneider, H.; Hoffbauer, W.; Jansen, M. *J. Non-Cryst. Solids* **1997**, *210*, 41–47.

(54) Smith, M. E.; van Eck, E. R. H. *Prog. Nucl. Magn. Reson. Spectrosc.* **1999**, *34*, 159–201.

(55) Alemany, L. B.; Kirker, G. W. *J. Am. Chem. Soc.* **1986**, *108*, 6158–6162.

(56) Fyfe, C. A.; Bretherton, J. L.; Lam, L. Y. *Chem. Commun.* **2000**, *2000*, 1575–1576.

(57) Iwasawa, Y. *Catal. Today* **1993**, *18*, 21–72.

(58) Campbell, C. T.; Parker, S. C.; Starr, D. E. *Science* **2002**, *298*, 811–814.

(59) Jaroniec, M.; Solovyov, L. A. *Langmuir* **2006**, *22*, 6757–6760.

(60) Yang, C.; Zibrowius, B.; Schmidt, W.; Schüth, F. *Chem. Mater.* **2004**, *16*, 2918–2925.

(61) Ryoo, R.; Kim, M. J. *Chem. Commun.* **1997**, *1997*, 2225–2226.

(62) Twigg, M. V.; Richardson, J. T. *Appl. Catal., A* **2000**, *190*, 61–72.

(63) Krawiec, P.; Weidenthaler, C.; Kaskel, S. *Chem. Mater.* **2004**, *16*, 2869.

(64) Sun, J.; Ma, D.; Zhang, H.; Liu, X.; Han, X.; Bao, X.; Weinberg, G.; Pfänder, N.; Su, D. *J. Am. Chem. Soc.* **2006**, *128*, 15756–15764.

(65) Wang, W.; Song, M. *Mater. Res. Bull.* **2006**, *41*, 436–447.

(66) Zheng, F.; Liang, L.; Gao, Y.; Sukamto, J. H.; Aardahl, C. L. *Nano Lett.* **2002**, *2*, 729–732.

(67) Huang, L.; Wind, S. J.; O'Brien, S. P. *Nano Lett.* **2003**, *3*, 299–303.

(68) Moshkalev, S. A.; Verissimo, C. *J. Appl. Phys.* **2007**, *102*, 044303–044303.

(69) Cantoro, M.; Hofmann, S.; Pisana, S.; Ducati, C.; Parvez, A.; Ferrari, A. C.; Robertson, J. *Diamond Relat. Mater.* **2006**, *15*, 1029–1035.

(70) Sohn, J. I.; Ok, Y.; Seong, T.; Lee, S. *J. Appl. Phys.* **2007**, *102*, 014301–014301.

(71) Campbell, C. T. *Surf. Sci. Rep.* **1997**, *27*, 3–111.

(72) Li, C.; Yao, K.; Liang, J. *Appl. Catal., A* **2004**, *261*, 221–224.

AM900625C